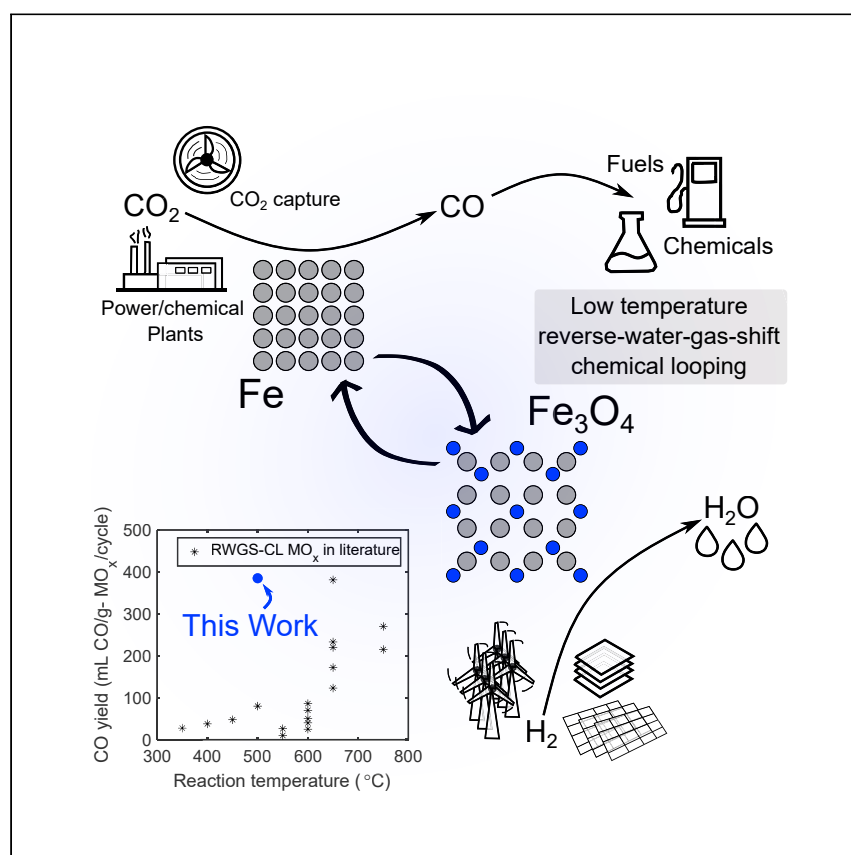Article

Low-temperature carbon dioxide conversion via reverse water-gas shift thermochemical looping with supported iron oxide

Eddie Sun, Gang Wan, Vasudev Haribal, ..., Jimmy Rojas, Raghubir Gupta, Arun Majumdar

amajumdar@stanford.edu

Highlights

Reverse water-gas shift chemical looping is demonstrated

High carbon monoxide yields with Fe_2O_3/ZrO_2 at low reaction temperature

Demonstration of good metal oxide stability for 12.1 days on stream

In situ X-ray characterization of a direct, reversible, and stable phase transition

Reverse water-gas shift chemical looping is a potentially scalable method for carbon dioxide utilization; however, achieving appreciable carbon monoxide yields and reaction rates at low reaction temperature remains a challenge. In this work, Sun et al. demonstrate the low-temperature performance of iron oxide featuring high carbon monoxide yields, fast kinetics, and great stability.

Article

Low-temperature carbon dioxide conversion via reverse water-gas shift thermochemical looping with supported iron oxide

Eddie Sun,[1] Gang Wan,[1] Vasudev Haribal,[2] Marco Gigantino,[3] Sebastian Marin-Quiros,[1] Jinwon Oh,[4] Arturas Vailionis,[5,6] Andrew Tong,[2] Richard Randall,[1] Jimmy Rojas,[1] Raghubir Gupta,[2] and Arun Majumdar[1,7,8,*]

SUMMARY

Carbon dioxide utilization via the reverse water-gas shift (RWGS) reaction is a potentially scalable method to mitigate rising global carbon dioxide emissions if high carbon monoxide yields and reaction rates can be achieved at low reaction temperatures. Iron oxide (Fe_2O_3) has been extensively studied as a chemical looping material in RWGS, but nearly all studies were performed at high temperatures, where sintering and deactivation occur. Here, we investigate Fe_2O_3 as an RWGS chemical looping metal oxide at low reaction temperatures (500°C for both oxidation and reduction steps) and find that a direct, reversible, and stable metal/oxide phase transition results in a high carbon monoxide yield of 386 mL CO/g-Fe_2O_3/cycle. The measured carbon monoxide yield remains relatively stable for 350 redox cycles or 12.1 days on stream. The affordability and abundance of Fe_2O_3, the high carbon monoxide yield, and its extended time-on-stream without substantial performance degradation makes Fe_2O_3 a RWGS chemical looping metal oxide with a promising chance of commercialization.

INTRODUCTION

CO_2 accumulation in the atmosphere due to fossil fuel combustion has resulted in a 1.2°C global average temperature increase since pre-industrial levels.[1] While efforts by industry, governments, and citizens alike to reduce CO_2 emissions are necessary and ongoing, it is also necessary to develop negative emissions technologies to mitigate hard-to-decarbonize industries. Today, while CO_2 has some uses, the total CO_2 demand is orders of magnitude below that of current CO_2 emissions (~40 Mt vs. ~40 Gt),[2] indicating that future negative emissions technologies must economically scale up to the Gt scale. Transforming CO_2 into chemicals and fuels should be part of the global negative emissions or net-zero emissions technology portfolio, especially since the chemicals and fuels industries can match the scale of CO_2 emissions.[3] In particular, thermochemical methods of CO_2 utilization using emissions-free heat and/or hydrogen should be explored since the chemicals and fuels industries at the Gt scale today rely almost exclusively on thermochemical systems.

CO_2 reduction to CO is the simplest reaction pathway to a useful product, as the produced CO can be used to synthesize methanol or long-chain hydrocarbons via the Fischer-Tropsch process. By using renewable hydrogen as the reducing agent via the reverse water-gas shift (RWGS) reaction

[1]Department of Mechanical Engineering, Stanford University, Stanford, CA 94305, USA

[2]Susteon, Inc., Cary, NC 27513, USA

[3]Department of Chemical Engineering, Stanford University, Stanford, CA 94305, USA

[4]Department of Materials Science and Engineering, Stanford University, Stanford, CA 94305, USA

[5]Stanford Nano Shared Facilities, Stanford University, Stanford, CA 94305, USA
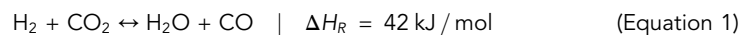
[6]Department of Physics, Kaunas University of Technology, 51368 Kaunas, Lithuania

[7]Precourt Institute for Energy, Stanford University, Stanford, CA 94305, USA

[8]Lead contact

*Correspondence: amajumdar@stanford.edu

https://doi.org/10.1016/j.xcrp.2023.101581

$$H_2 + CO_2 \leftrightarrow H_2O + CO \quad | \quad \Delta H_R = 42\,kJ/mol \qquad \text{(Equation 1)}$$

on heterogeneous catalysts, CO_2 can be thermochemically reduced to CO at reaction temperatures below 600°C.[4] However, for chemicals and fuels production, further efforts should be pursued to further decrease the RWGS reaction temperature closer to the reaction temperature of methanol and Fischer-Tropsch synthesis (<350°C) to increase energy efficiency and reduce capital costs and for ease of reactor system management. In addition, catalytic RWGS processes produce CH_4 as an undesired by-product at temperatures below 600°C,[4] which hinders further reductions in reaction temperature. Recent work has achieved high CO selectivity at reaction temperatures below 600°C with specially designed catalysts[5–7]; however, CO_2 conversion in catalytic RWGS systems at low temperatures is low: at a reaction temperature of 500°C, atmospheric pressure, and an H_2/CO_2 mole fraction ratio of 3, CO_2 conversion is only approximately 8%.[8]

Chemical looping RWGS (RWGS-CL) converts CO_2 into CO at potentially lower temperatures than catalytic RWGS with near 100% CO selectivity.[4] The RWGS-CL process consists of the following two cyclic reactions:

$$MO_x + H_2 \rightarrow MO_{x-\delta} + H_2O \qquad \text{(Equation 2)}$$

$$MO_{x-\delta} + CO_2 \rightarrow MO_x + CO \qquad \text{(Equation 3)}$$

where MO_x represents a metal oxide and $MO_{x-\delta}$ represents a reduced metal oxide. By physically separating the hydrogen from the carbon oxides, CH_4 formation is completely avoided. This allows for the further reduction of reaction temperature compared to catalytic RWGS, as long as appreciable reaction rates can still be achieved.

The RWGS process requires that H_2 be affordable and produced without CO_2 emissions. However, we expect that this will indeed occur in the future, as steam methane reforming with carbon capture, electrolysis, and methane pyrolysis technologies to produce clean H_2 continues to mature. In fact, it is the purpose of the US Department of Energy's "Hydrogen Earthshot" initiative to develop the technology to produce emissions-free H_2 at $1/kg-$H_2$ by 2030.[9]

Previously reported RWGS-CL metal oxides with high CO yields include supported Fe_2O_3,[10–16] lanthanum-based perovskites,[15,17–23] and transition-metal-doped ferrites.[16,24–27] CO yields generally increase with increasing reaction temperature, with the highest reported yields being ~381 mL CO/g-MO_x/cycle at 650°C by Zhao et al.,[15] ~86 mL/CO/g-MO_x/cycle at 600°C by Jo et al.,[19] and ~47 mL CO/g-MO_x/cycle at 450°C by Castellanos-Beltran et al.[26]; however, it is necessary to note that all experiments are performed with differing H_2 and CO_2 feed gas concentrations, reactor setups, experimental procedures, sample surface area, etc., making direct comparisons difficult. Using CH_4 or other hydrocarbon fuels as reductants in place of hydrogen is more economically affordable but generally results in lower yields, has challenges related to coking, and requires higher reaction temperatures.[28,29] Much progress has been made to maintain high reaction rates while lowering the reaction temperature; however, more research on materials discovery is required to achieve commercially viable reaction rates at lower reaction temperatures.

Fe_2O_3 in particular is a metal oxide that has been extensively studied not only for RWGS-CL but for CL systems in general.[30,31] However, to the best knowledge of
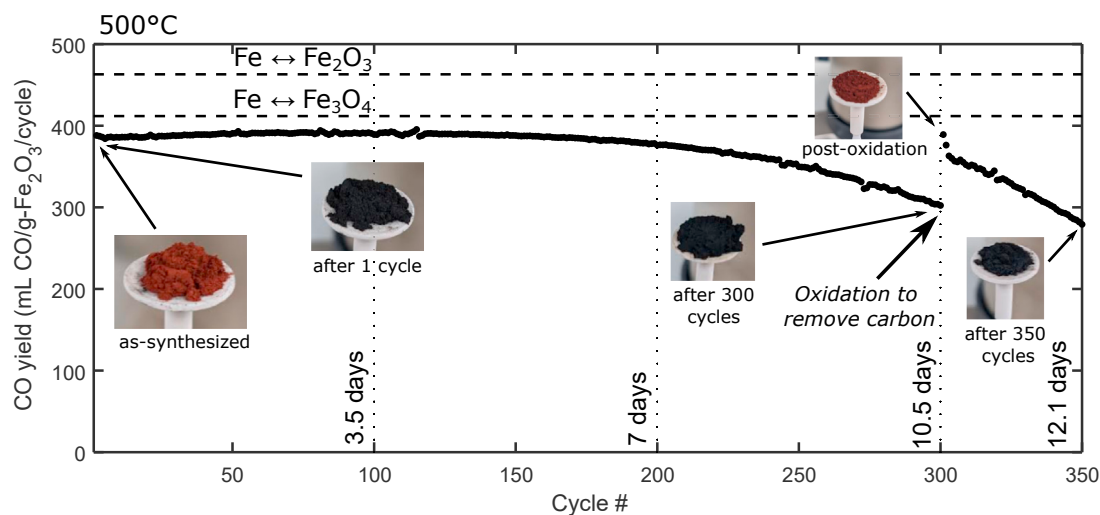
Figure 1. Fe$_2$O$_3$/ZrO$_2$ RWGS-CL redox performance and physical state throughout cycling
CO yield in 350 cycles (12.1 days on stream) of TGA cycling at 500°C with sample images at various points during cycling. An oxidation step to remove produced carbon was performed at cycle 300. Theoretical CO yields from Fe/Fe$_3$O$_4$ and Fe/Fe$_2$O$_3$ redox couples are denoted by the dotted lines.

the authors, there have been few CL studies including with Fe$_2$O$_3$ at low temperatures (<550°C).[26,32,33] This is likely because higher reaction temperatures are favorable for both the thermodynamics and kinetics of RWGS-CL and other CL processes, especially studies involving CH$_4$ as a reductant, which requires high temperatures to activate. However, high reaction temperatures result in metal oxide deactivation and sintering caused by repeated redox cycling at elevated temperatures above the Tamman temperature of iron and iron oxides. The rate of decrease in surface area has been previously shown to be Arrhenius in nature[34]; therefore, lowering the reaction temperature results in sintering occurring at an exponentially slower rate. The challenge thus far, however, is to achieve appreciable CO yields per cycle and fast reaction kinetics at these low reaction temperatures.

Here, in this work, we show that reducing the reaction temperature to 500°C for both oxidation and reduction steps of ZrO$_2$-supported Fe$_2$O$_3$ still can achieve a high CO yield (386 mL CO/g-Fe$_2$O$_3$/cycle) with surprisingly fast kinetics and low decay in activity over 350 redox cycles (12.1 days on stream). This CO yield of 386 mL CO/g-Fe$_2$O$_3$/cycle is higher than those of previously reported metal oxides in the literature at low reaction temperatures, suggesting that Fe$_2$O$_3$ possesses promising low-temperature RWGS-CL potential. We observed the slow, gradual formation of carbon on Fe$_2$O$_3$/ZrO$_2$ due to the Boudouard reaction (2CO $\rightarrow$ CO$_2$ + C) from excess CO production, which has not been previously observed in RWGS-CL to the best knowledge of the authors. We also characterized Fe$_2$O$_3$/ZrO$_2$ using X-ray diffraction (XRD) and X-ray absorption spectroscopy (XAS) and identified that a direct, reversible, and stable (Fe$_3$O$_4$) to metallic (Fe) phase swing in Fe$_2$O$_3$/ZrO$_2$ is responsible for its noteworthy CO yield. We hypothesize that the high CO yield and fast kinetics at 500°C is due to the lack of much reaction-rate-limiting FeO formation during the Fe to Fe$_3$O$_4$ phase swing.

RESULTS AND DISCUSSION
Redox cycling performance
We experimentally measured the CO yield of the Fe$_2$O$_3$/ZrO$_2$ metal oxide via redox cycling using thermogravimetric analysis (TGA) (Figures 1 and S1). Due to calcination

at 1,000°C in air during synthesis, the Fe_2O_3/ZrO_2 metal has a starting Fe phase of Fe_2O_3 (the sample henceforth is referred to as Fe_2O_3/ZrO_2 even if the Fe phase is not Fe_2O_3). We verified the Fe weight loading and checked for impurities via X-ray fluorescence measurements (Figure S2), characterized the morphology of the particles via microscopy (Figure S3), verified that the ZrO_2 support exhibits no oxygen exchange capacity (Figure S4), and measured the specific surface area of the as-synthesized Fe_2O_3/ZrO_2 metal oxide (3.1 m^2/g; Figure S5). Representative TGA cycling data are shown in Figure S6. All weight changes of the Fe_2O_3/ZrO_2 were assumed to be solely due to redox-induced oxygen transfer; this assumption was verified by gas chromatography (Figures S7A and S7B).

The results of TGA redox cycling are shown in Figure 1. From cycles 1 to 300, we performed RWGS-CL cycling as described in the previous paragraph (Figures 1 and S8). The Fe_2O_3/ZrO_2 metal oxide produced nearly 400 mL CO/g-Fe_2O_3/cycle, which gradually decreased to 300 mL CO/g-Fe_2O_3/cycle by the 300th cycle. After removing the sample from the reactor after the 300th cycle, we observed the formation of carbon on the Fe_2O_3/ZrO_2 metal oxide in the form of disordered graphitic sheets (Figures 1 and S9). Between cycles 1 and 300, 452 mg C/g-Fe_2O_3 was produced in total (1.5 mg C/g-Fe_2O_3/cycle), a small amount compared with the amount of produced CO (~400 mg CO/g-Fe_2O_3/cycle). To remove the carbon, we performed an oxygen oxidation on the sample. Following this oxidation step, we performed 50 additional RWGS-CL cycles, resulting in 350 total redox cycles performed and a total of 12.1 days on stream at 500°C (Figures 1 and S10). The Fe_2O_3/ZrO_2 metal oxide produced nearly 400 mL CO/g-Fe_2O_3/cycle again in the 301st cycle post-carbon oxidation but decreased to 275 mL CO/g-Fe_2O_3/cycle by cycle 350. We attribute the decrease in activity with increased cycle time primarily to carbon formation blocking H_2 and CO_2 access to the Fe_2O_3 or to sintering of the Fe_2O_3 due to local temperature hotspots resulting from the exothermic oxidation process performed after cycle 300. It is worth noting that the rate of decay with increased cycling is faster in cycles 300–350 (Figures 1 and S10). Chemical and physical changes to the metal oxide such as slow sintering may be occurring, thus affecting mass transfer of oxygen species through the oxide; this should be studied as part of future work.

The formation of carbon on the Fe_2O_3/ZrO_2 metal oxide is due to the Boudouard reaction:

$$2\,CO \leftrightarrow CO_2 + C \quad | \quad \Delta H_R = -170\,kJ/mol. \qquad \text{(Equation 4)}$$
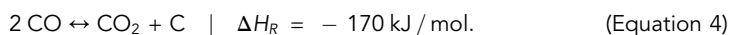
The Boudouard reaction is strongly exothermic, and thus the forward reaction is favorable at low temperatures. At 500°C, the equilibrium ratio of CO to CO_2 (and C) is 1.1% (Figure S11). This means that the production of CO via RWGS-CL resulting in greater than 1.1% CO concentration creates an environment that is thermodynamically favorable for carbon formation, although the reaction kinetics at 500°C could be slow. To the best of the knowledge of the authors, this is the first report of carbon formation in the RWGS-CL process. We hypothesize that this is the case because (1) most previous RWGS-CL studies were performed at higher reaction temperatures, where carbon formation is less thermodynamically favorable, and (2) absolute RWGS-CL CO yields were comparatively lower.

We observed a phase swing in Fe_2O_3/ZrO_2 between Fe_3O_4 and metallic Fe during redox cycling. The experimentally measured 386 mL CO/g-Fe_2O_3/cycle yield of Fe_2O_3/ZrO_2 is close in value to the theoretical CO yield of 412 mL CO/g-Fe_2O_3/cycle for a Fe_3O_4/Fe redox couple (Figure 1). Although the starting state is Fe_2O_3 (which is an orange color), the sample appears dark gray after one redox cycle, which is typical
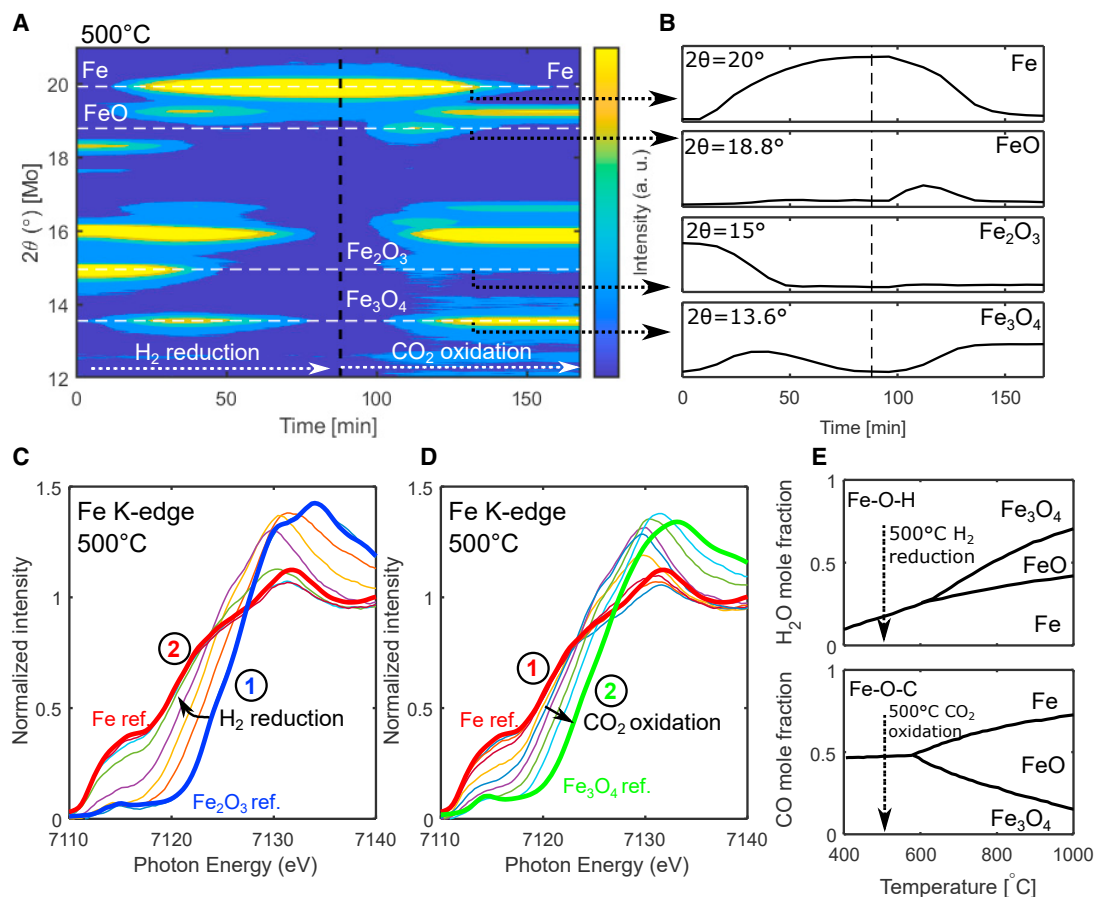
Figure 2. *In situ* XRD on unsupported Fe_2O_3, indicating the presence of an Fe/Fe_3O_4 redox couple
(A) Unlabeled diffraction peaks are duplicates of already labeled diffraction peaks (Figure S12).
(B) *In situ* XRD slices showing the relative intensity at specified 2θ angles corresponding to phases of Fe oxides. A small amount of FeO is observed as an intermediate between Fe and Fe_3O_4.
(C and D) *In situ* Fe K-edge XAS during (C) H_2 reduction and (D) CO_2 oxidation of Fe_2O_3/ZrO_2, again indicating the presence of an Fe/Fe_3O_4 redox couple.
(E) Equilibrium phase diagram of the Fe-O-H (top) and Fe-O-C (bottom) systems. At an RWGS-CL reaction temperature of 500°C, FeO formation is not thermodynamically favorable.

of Fe_3O_4 (Figure 1). Fe_2O_3 does not appear again until after the 300th cycle, following the oxidation of coke (and Fe_3O_4) with air (Figure 1). This is consistent with previous RWGS-CL work on Fe_2O_3 as an oxygen carrier stating that CO_2 cannot oxidize Fe to Fe_2O_3 and can only oxidize Fe to Fe_3O_4.[10–13] Similarly, after the 350 redox cycles, the sample appears dark gray again, indicating the presence of Fe_3O_4 (Figure 1).

Fe_2O_3 phase swing and intermediate phases during RWGS-CL redox cycling
The Fe_3O_4/Fe phase swing was directly confirmed by *in situ* XRD (Figures 2A, 2B, and S12) and *in situ* X-ray absorption near-edge fine structure (XANES) at the Fe K-edge (Figures 2C and 2D). *In situ* XRD indicates a Fe_2O_3 (2θ = 15°) to Fe_3O_4 (2θ = 13.6°) to Fe (2θ = 20°) phase transition in the 1st H_2 reduction cycle (Figures 2A, 2B, and S12), followed by a Fe to Fe_3O_4 phase transition during CO_2 oxidation (Figures 2A, 2B, and S12). The full Fe_3O_4 to Fe phase swing allows for the maximum utilization of the oxygen capacity of Fe; much more CO is produced from an Fe_3O_4/Fe phase swing as opposed to an Fe_3O_4/FeO phase swing.
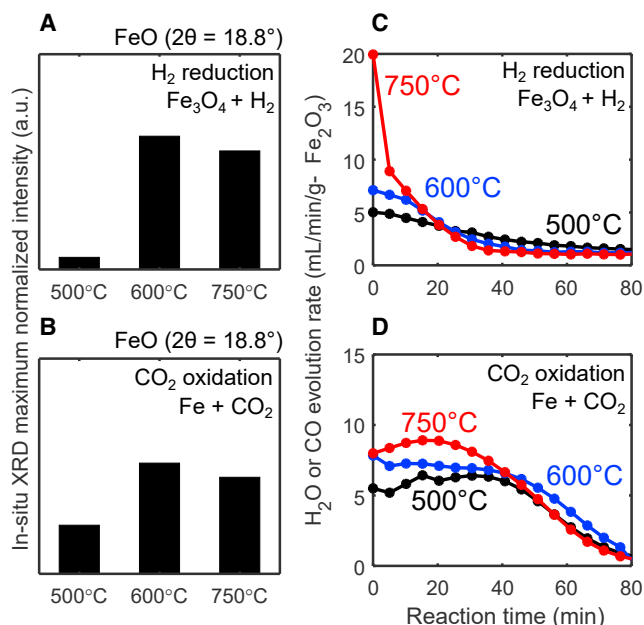
Figure 3. Relative intensity of the *in situ* XRD FeO peak

(A and B) Maximum relative intensity of the FeO peak (at $2\theta = 18.8°$) during (A) H_2 reduction and (B) CO_2 oxidation of unsupported Fe_2O_3 at 500°C–750°C reaction temperatures. FeO formation is lowest at 500°C.

(C and D) Comparison of (C) 5% H_2/Ar reduction and (D) 5% CO_2/Ar oxidation reaction rate of Fe_2O_3/ZrO_2 at 500°C–750°C reaction temperatures. Note that dilute gases were used in packed-bed experiments as opposed to pure gases in TGA experiments. H_2 reduction rate benefits from higher reaction temperature (likely due to more favorable thermodynamics); CO_2 oxidation rate does not increase much with temperature.

At a reaction temperature of 500°C, a small amount of FeO formation ($2\theta = 18.8°$) (and subsequent disappearance) was observed as an intermediate state between Fe and Fe_3O_4 (Figures 2A, 2B, 3A, and 3B), despite FeO formation being thermodynamically unfavorable at 500°C according to Fe–O–H and Fe–O–C system phase diagrams (Figure 2E). This observation of FeO as an intermediate, metastable phase is consistent with previous literature[10–13,24]: at reaction temperatures below 450°C, FeO formation is avoided, and $Fe_3O_4 \leftrightarrow$ Fe proceeds directly.[35–37] Between 450°C and 570°C, FeO and Fe form simultaneously via $Fe_3O_4 \leftrightarrow$ Fe + FeO $\leftrightarrow$ Fe,[35–37] which we observed (Figures 2A, 2B, and S12–S16). However, FeO formation is least prevalent at a reaction temperature of 500°C compared with at higher reaction temperatures of 600°C and 750°C (Figures 3A, 3B, and S12–S16). In addition, local "hot spots" in the XRD *in situ* reaction cell due to inhomogeneous heating may have caused additional FeO formation.

We hypothesize that the avoidance of FeO formation at 500°C results in higher-than-expected reaction rates as measured by gas chromatography in a packed-bed u-tube reactor (Figures 3C and 3D). Rate measurements were performed on Fe_2O_3/ZrO_2 with dilute 5% H_2/Ar and 5% CO_2/Ar and with SiC as a metal oxide diluent to ensure that neither mass nor heat diffusion affected the kinetic measurement results. The gas-phase reaction between iron oxides and H_2 has been extensively previously studied,[35,36,38] and it is generally accepted that the apparent activation energy and/or reaction rate of the Fe_3O_4 reduction increases above 570°C.[38,39] (Interestingly, the gas-phase reaction between metallic Fe and CO_2
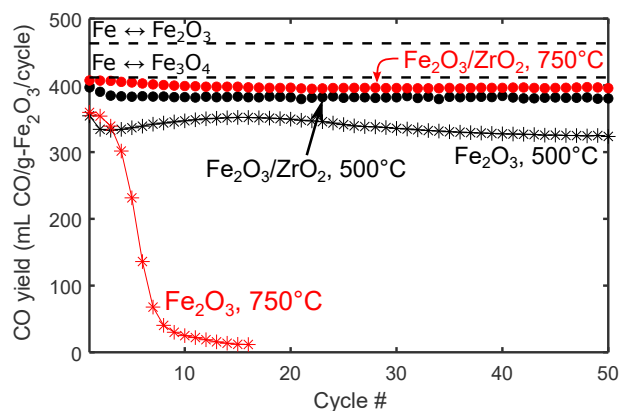
Figure 4. Effect of the ZrO₂ support and reaction temperature on long-term Fe₂O₃/ZrO₂ RWGS-CL stability

Unsupported Fe₂O₃ at a reaction temperature above the Tamman temperature of Fe (approximately 600°C) has poor stability due to sintering. Theoretical CO yields from Fe/Fe₃O₄ and Fe/Fe₂O₃ redox couples are denoted by the dotted lines.

has been studied considerably less.) The Fe_3O_4 to FeO phase transition specifically has been previously reported to have higher activation energies for reduction and oxidation reactions than the Fe_3O_4 to Fe and FeO to Fe phase transitions,[37] although variation exists in previous work.[35] While the H_2 reduction rate benefits from higher reaction temperature (Figure 3C), likely due to more favorable thermodynamics since H_2 reduction of Fe_3O_4 is strongly endothermic (Figures S17A and S17B), the CO_2 oxidation rate does not increase much with temperature (Figure 3D). The lack of an expected exponential (Arrhenius) rate dependence on temperature could be attributed to the crossing (and avoidance) of the comparatively high activation energy $Fe_3O_4 \leftrightarrow FeO$ and/or $FeO \leftrightarrow Fe$ phase transition.

Sintering, long-term metal oxide stability, and the optimal operating temperature window

Fe_2O_3 is known to sinter rapidly in CL processes,[34,40] but the Fe_2O_3/ZrO_2 metal oxide reported here exhibits good stability at 500°C reaction temperature, as evidenced by its remarkable CO yield retention (>75%) for up to 12.1 days on stream. *Ex situ* XRD, near-edge X-ray absorption fine structure (NEXAFS) at the Fe L-edge, and scanning electron microscopy (SEM) showed no obvious structural or phase changes between 1 and 350 cycles (Figures S18–S20). We attribute this lack of sintering to (1) the reaction temperature of 500°C being well below the Tamman temperature of Fe (approximately 600°C),[41] (2) the ZrO_2 support, which anchors the Fe_2O_3, (3) the low surface area of the sample (Figure S5), and (4) the avoidance of FeO formation, which has been previously reported to induce sintering.[42]

We examined this hypothesis by performing TGA redox cycling experiments on the Fe_2O_3/ZrO_2 to induce sintering by (1) removing the ZrO_2 support and (2) increasing the reaction temperature to 750°C, which is above the Fe Tamman temperature (Figure 4). At 500°C, both unsupported and supported Fe_2O_3 exhibit good stability up to 50 cycles (3.5 days on stream). However, at 750°C, while the ZrO_2-supported Fe_2O_3 exhibits good stability, the CO yield of unsupported Fe_2O_3 decreases rapidly, which is consistent with previous literature.[34,40] Direct evidence of sintering is seen in SEM imaging (Figure S21). We hypothesize that the lack of dispersion of the unsupported Fe_2O_3 may have caused some Fe_2O_3 near the core of a particle to become inactive and thus not participate in the redox reaction, resulting in a slightly lower
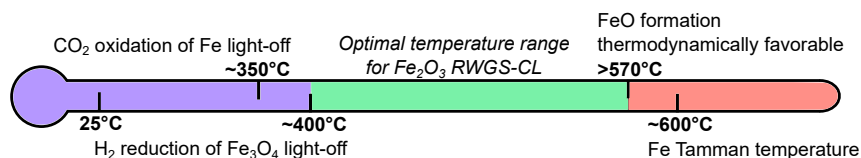
Figure 5. Proposed idea of an optimal temperature range for Fe₂O₃ RWGS-CL

Low-temperature Fe_2O_3 RWGS-CL is infeasible due to slow kinetics, while high temperature Fe_2O_3 RWGS-CL is more challenging due to sintering and overcoming slower reaction rates from FeO formation.

CO yield than the supported sample; CO_2 may have had difficulty accessing the deeply embedded Fe_2O_3 in the particles.

Previous work in RWGS-CL on Fe_2O_3 has almost exclusively focused on enhancing Fe_2O_3 stability via engineering the support, e.g., by doping with one or multiple transition metals or through the design of the microstructure.[10–12,14,15,24] Enhancing Fe_2O_3 stability for the aforementioned studies was necessary due to RWGS-CL operation at high reaction temperatures above the Fe Tamman temperature. However, our data suggest that Fe_2O_3 RWGS-CL with appreciable reaction rates may not require high reaction temperatures. In fact, a lower reaction temperature avoids sintering and may also be advantageous due to the avoidance of reaction-rate-limiting FeO formation as stated in the previous section. Lower RWGS-CL reaction temperatures are also beneficial from a commercialization perspective since the reaction temperature of downstream methanol and Fischer-Tropsch synthesis is comparatively low (<350°C). Simpler metal oxide designs with a smaller number of transition metals and less structural requirements are also considerably easier and cheaper to synthesize on industrial production scales. While direct comparison between different studies is difficult due to different gas compositions, reactor configurations, and experimental procedures used, we suggest that more future work to increase reaction kinetics such as microstructural support engineering and modifying physical and chemical properties of the metal oxide be pursued at low reaction temperatures (below the Fe Tamman temperature) as opposed to at high reaction temperatures.

Since sintering and FeO formation effectively place a "soft ceiling" on the Fe_2O_3 RWGS-CL reaction temperature, we propose the idea that there exists an optimal operating temperature range for Fe_2O_3 RWGS-CL (Figure 5). (We use the term "soft ceiling" since sintering can be mitigated with a strong support material like ZrO_2.) The "soft" reaction temperature "ceiling" is approximately 570°C since FeO formation is thermodynamically favorable above this temperature. In addition, the Fe Tamman temperature is approximately 600°C, although sintering can be substantially limited with the addition of a support. Conversely, Fe_2O_3 RWGS-CL is limited at low temperatures by slow kinetics. The reaction temperature "floor" is approximately 400°C (Figures S22A–S22D), as determined by temperature-programmed H_2 reduction (TPR) and CO_2 oxidation (TPO). 400°C is the approximate temperature at which the H_2 reduction of Fe_3O_4 begins to occur (Figure S22C).

Comparison with previously reported RWGS-CL metal oxides in the literature

We compared the Fe_2O_3/ZrO_2 performance reported in this work with other RWGS-CL metal oxides previously reported in the literature (Figure 6A; Table S1) with isothermal CO_2 oxidation and H_2 reduction reaction temperatures.[10,12,14–20,22–27,32,43] CO yield
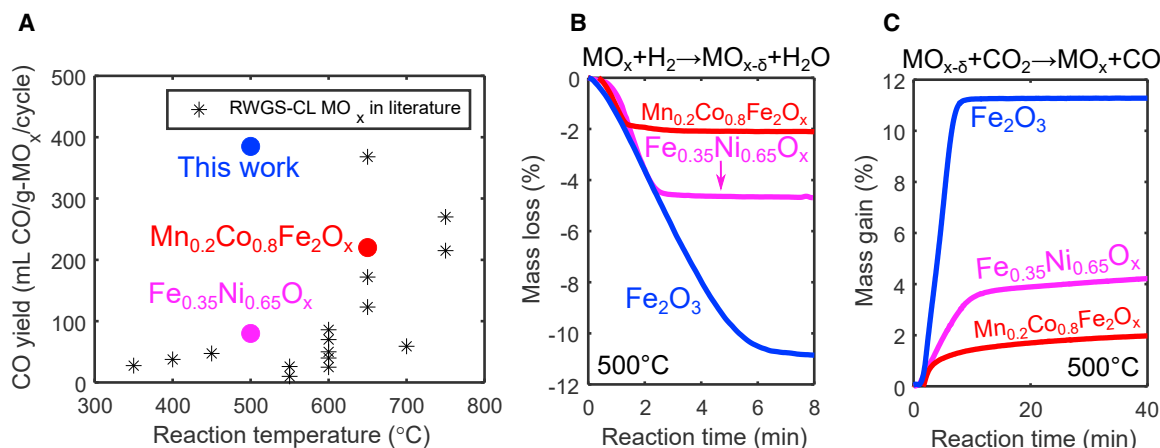
Figure 6. Comparison with previously reported RWGS-CL metal oxides

(A) CO yield of previously reported RWGS-CL metal oxides normalized by the metal oxide mass (note: the weight of the support, if present, is ignored).[10,12,14–20,22–26,32,43] $FeNiO_x$[27] and $Mn_{0.4}Co_{0.6}Fe_2O_4$[25] denoted by pink and red dots, respectively, are the most promising non-Fe_2O_3-based RWGS-CL metal oxides previously reported and thus were selected for direct comparison at 500°C.

(B and C) Comparison of (B) TGA H_2 reduction and (C) TGA CO_2 oxidation of the three metal oxides. All metal oxides are 40% MO_x/60% ZrO_2 by weight and were previously redox cycled once. The H_2 reduction rate is similar between the three metal oxides, but Fe_2O_3 has a considerably faster CO_2 oxidation rate.

generally increases with increasing reaction temperature, with the highest non-Fe_2O_3 metal oxide reported yields being ~220 mL CO/g-MO_x/cycle at 650°C by Ma et al.,[25] ~86 mL/CO/g-MO_x/cycle at 600°C by Jo et al.,[19] and ~47 mL CO/g-MO_x/cycle at 450°C by Castellanos-Beltran et al.[26]; however, we note that all experiments are performed with differing H_2 and CO_2 feed gas concentrations, reactor setups, experimental procedures, sample surface areas, etc., making direct comparisons difficult.

We directly compared the RWGS-CL performance of Fe_2O_3/ZrO_2 at 500°C in this work with the RWGS-CL performance of $Fe_{0.35}Ni_{0.65}O_x$[27] and $Mn_{0.4}Co_{0.6}Fe_2O_4$[25] denoted by the pink and red points in Figure 6A, respectively, as these two non-Fe_2O_3-based metal oxides possess high CO yields at their reported respective reaction temperatures relative to other metal oxides. The $Mn_{0.4}Co_{0.6}Fe_2O_4$ and $Fe_{0.35}Ni_{0.65}O_x$ samples for TGA redox cycling were synthesized using the same synthesis method as that of Fe_2O_3; ZrO_2 was used as the support (40% MO_x/60% ZrO_2 by weight) for all three metal oxides. TGA cycling experiments at 500°C were performed with the same experimental procedure as that of Fe_2O_3/ZrO_2. The samples were redox cycled once to set the starting phase for redox cycling (e.g., Fe_3O_4 for Fe_2O_3/ZrO_2), and the second redox cycle was used for comparison.

We observed that the H_2 reduction rate of the three metal oxides is approximately the same (Figure 6B) but that Fe_2O_3/ZrO_2 possesses a faster CO_2 oxidation rate compared with $Mn_{0.4}Co_{0.6}Fe_2O_4$/ZrO_2 and $Fe_{0.35}Ni_{0.65}O_x$/ZrO_2 (Figure 6C). More importantly, the oxygen capacity of Fe_2O_3/ZrO_2 per cycle is considerably higher than those of $Mn_{0.4}Co_{0.6}Fe_2O_4$/ZrO_2 and $Fe_{0.35}Ni_{0.65}O_x$/ZrO_2 due to the $Fe_3O_4 \leftrightarrow$ Fe redox couple of Fe_2O_3/ZrO_2 (Figures 6B and 6C). Although we again note that direct comparisons between different studies is difficult and that only the three best-performing metal oxides (as subjectively determined by the authors) were compared here, the data suggest that Fe_2O_3/ZrO_2 has a high CO compared with previously reported RWGS-CL metal oxides and that it possesses comparatively fast kinetics.

Extension of low-temperature RWGS-CL to the direct reduction of iron

H_2 reduction of the Fe_2O_3 without ZrO_2 as a support is the direct reduction of iron (DRI) process, which has been proposed as a possible technology to assist the decarbonization of steel production. Today, the first step of steel production is the reduction of iron oxides to pig iron (composted of mostly metallic iron) using carbon monoxide (from coal products reacted with oxygen) as the reducing agent, resulting in large amounts of CO_2 emissions. DRI with hydrogen as the reductant has the potential to reduce CO_2 emissions and could operate at smaller production scales, allowing for decentralized production.

We observed that unsupported Fe_2O_3 possessed similar RWGS-CL performance compared with Fe_2O_3/ZrO_2 at a $500°C$ reaction temperature (Figure 4), suggesting that the RWGS-CL reaction rate temperature dependence of Fe_2O_3 should not be much different than what was observed in Fe_2O_3/ZrO_2 (below the Fe Tamman temperature). Therefore, we hypothesize that low-temperature DRI (i.e., at $500°C$ reaction temperature) may have higher-than-expected reaction rates. For low-temperature DRI, reduction with H_2 as the reducing agent is not advantageous at low temperatures due to the high endothermicity of reaction (Figures 3C, S17A, and S17B). However, CO reduction of Fe_2O_3 could be advantageous at low temperatures since CO reduction of Fe_2O_3 is an exothermic reaction. This would be in contrast to today's blast furnaces, which operate at high temperatures (>$900°C$). We note that a small amount of O_2 should be co-fed with CO to avoid coking due to the favorable thermodynamics of the Boudouard reaction at low temperatures (Figure S11). While this is out of the scope of the current work, reaction rate measurements vs. reaction temperatures coupled with *in situ* X-ray characterization and electron microscopy methods for the purpose of studying low-temperature DRI should be pursued as part of future work.

To conclude, in this work, we investigated the low-temperature capability ($500°C$) of Fe_2O_3 in CO_2 conversion to CO in an RWGS-CL process and demonstrated 350 cycles or 12.1 days on stream at high CO yields (386 mL CO/g-Fe_2O_3/cycle). This CO yield of 386 mL CO/g-Fe_2O_3 is the highest CO yield reported at a $500°C$ reaction temperature. We found that a direct, complete, reversible, and fast spinel to metallic phase change is responsible for its high oxygen capacity as examined by *in situ* XRD and XAS. We also observed via XRD and XAS that little FeO formation occurs at $500°C$ compared with at higher reaction temperatures, and we hypothesize that the lack of FeO formation is responsible for the higher-than-expected CO_2 reduction kinetics that were observed.

These results suggest that the cost of CO production at low reaction temperatures ($500°C$) could be lower than CO production at high reaction temperatures (~$750°C$): capital expenditures (CAPEXs) of an RWGS-CL chemical plant operating at a low maximum temperature of $500°C$ will have considerably lower CAPEXs than a chemical plant operating at higher temperatures by avoiding the use of expensive, temperature-resistant materials such as Ni-based alloys, Inconel, and/or stainless steel that also need to be tolerant to the highly reducing environment of this process. However, it is important to note that the gas-phase conversion of both H_2 reduction and CO_2 oxidation reactions is lower at $500°C$ than at higher temperatures; a full technoeconomic analysis comparing the cost of CO production at high and low temperatures should be pursued as future work. We also note here that this RWGS-CL process with Fe_2O_3 may be a prime candidate for the use of induction heating, as all phases of Fe present during RWGS-CL are ferromagnetic, and the process operates at a temperature well below the Curie temperature of

Fe ($\sim$770°C). These factors, coupled with the affordability and abundance of Fe_2O_3 and its fast kinetics, high CO yield, and extended time-on-stream without substantial performance degradation, make Fe_2O_3 the RWGS-CL metal oxide with a promising chance of commercialization.

EXPERIMENTAL PROCEDURES

Resource availability

Lead contact

Further information and requests for resources should be directed to and will be fulfilled by the lead contact, Arun Majumdar (amajumdar@stanford.edu).

Materials availability

This study did not generate new materials.

Data and code availability

The data presented in this work are available from the corresponding authors upon reasonable request.

Fe_2O_3/ZrO_2 synthesis

Fe_2O_3/ZrO_2 samples were synthesized using the following procedure: iron(III) nitrate nonahydrate ($\geq$98%, Sigma-Aldrich) and ZrO_2 powder ($\geq$99%, Sigma-Aldrich, 5 μm) were dissolved in deionized (DI) water with the following precursors: (1) water = 1:4 in mass of Fe nitrate precursor, (2) EDTA (ethylenediamine tetraacetic acid; Sigma-Aldrich), and (3) citric acid ($\geq$99.5%, Sigma-Aldrich) were added to the solution with 60% and 75% the total molar amount of Fe ions, respectively. (For example, if there was 1 mol Fe nitrates in total, 0.6 mol EDTA and 0.75 mol citric acid would be added.) With 300 rpm stirring, ammonium hydroxide solution (28%–30%, Fisher Chemical) was added until pH = 11, forming a dark solution. The amount of ZrO_2 was measured so that its mass would be 60% of the final mixture of Fe_2O_3/ZrO_2.

The resulting solution was stirred and heated on a hot plate at 200°C for about 5 h (gelation). The spin bar was then removed, and the hot plate temperature was increased to 400°C to dry the gel overnight, during which foaming occurred and fluffy solid residues formed. The sample was then ground into powder, transferred to an alumina boat, and calcined in air with the following temperature program: 10°C/min until 800°C and 5°C/min until 1,000°C, held for an hour, 5 °C/min until 800°C, and then natural cooling.

Redox cycling experiments

TGA experiments were performed in a simultaneous thermal analyzer NETZSCH STA 449 F3 Jupiter thermal gravimetric analyzer fed by 99.999% purity Ar, CO_2, and H_2 obtained from Praxair USA. In a typical experiment, we placed $\sim$100 mg sample in an Al_2O_3 plate and fed Ar, CO_2, or H_2 gas as desired. The TGA always requires an additional 25 sccm protective flow of Ar. The partial pressure of O_2 (p_{O2}) measurements were performed using a Zirox ZR5 oxygen sensor. The p_{O2} was measured using a Zirox ZR5 p_{O2} sensor at 10^{-25} atm during H_2 reduction and at 10^{-20} atm during CO_2 oxidation. Correction runs without any sample were performed as needed to account for the weight changes due to changes in gas flow, temperature, and valve changes. A typical experimental was as follows: 40°C/min temperature ramp in 125 sccm Ar to 500°C (or the desired reaction temperature), 125 sccm H_2 reduction until equilibrium (typically 20 min), 5 min of 125 sccm Ar purge, 75 sccm CO_2 oxidation until equilibrium (typically 20 min), 5 min of 125 sccm Ar purge, redox cycling as previously described for the prescribed number of cycles, and a final 125 sccm Ar

cooldown at 40°C/min to room temperature. Gas chromatography was used to ensure that no air (oxygen) leaks were present.

Fixed-bed reaction rate measurements were performed in a U-shaped quartz micro-reactor with an internal diameter of 1 cm to give an oxide bed length of about 1 cm. The reactor was fed by ultra-high-purity dilute gases obtained from Airgas USA: 100 sccm 5% H_2/Ar, 150 sccm 5% CO_2/Ar, and 100 sccm Ar (for purging of the reactor). Typically, 100 mg Fe_2O_3/ZrO_2 and 100 mg SiC as a dilutant were placed between two layers of granular quartz, which were used for preventing displacement of the catalyst powder and for pre-heating the reactant gases. Usage of dilute gases, SiC as a dilutant, and operation at low H_2 and CO_2 conversions was to ensure that the reaction rate measurement was not affected by heat and mass transfer limitations (H_2 and CO_2 conversions are shown in Figure S23). The reactor was heated by a Micromeritics ChemiSoft TPx system furnace, and the temperature was recorded by a K-type thermocouple inserted inside the catalytic bed. All experiments were conducted at atmospheric pressure. In a typical experiment, the reaction steps were as follows: (1) reactor heated up in Ar to the desired reaction temperature; (2) H_2 reduction at the desired reaction temperature until no more H_2 was consumed (i.e., FeO_x is fully reduced to Fe); (3) Ar purging to remove remaining H_2 in the reactor; (4) CO_2 oxidation at the desired reaction temperature until no more CO_2 was consumed (i.e., Fe is fully oxidized to Fe_3O_4); (5) Ar purging to remove remaining CO_2 in the reactor; (6) repetition of steps 2–4 as desired; and (7) cool down of the reactor in Ar. The downstream gas composition was monitored using a mass spectrometer (Hiden HPR20) following the parent molecular ions for H_2 (mass 2), H_2O (mass 18), CO (mass 28), and CO_2 (mass 44) and/or an online multiple gas analyzer MG#5 gas chromatograph purchased from SRI instruments equipped with a thermal conductivity detector and a flame ionization detector with a methanizer using Ar as a carrier gas.

Materials characterization

Ex situ symmetrical 2θ-θ XRD experiments in Bragg-Brentano geometry were performed using a PANalytical B.V. Empyrean X-ray Diffractometer using a Cu source (λ = 1.5419 Å), iCore incident beam optics, and GaliPIX-3D detector in 1D static line detector mode. A Mo source (λ = 0.7107 Å) and an Anton-Paar XRK-900 stainless-steel reaction chamber were used for *in situ* XRD experiments with dilute H_2 and CO_2 gases. SEM images were collected using an FEI Magellan 400 XHR with a field-emission gun source and a Thermo Fisher Scientific Apreo S LoVac microscope. Both were used in secondary electron detection modes. Transmission electron microscope images were collected using an FEI Tecnai G2 F20 X-TWIN system operating at 200 kV. Samples were prepared by drop casting dilute ethanol dispersions of Fe_2O_3/ZrO_2 directly onto Cu grids. X-ray fluorescence data were collected using a Spectro Xepos HE XRF Spectrometer. Raman spectroscopy was performed using a HORIBA Scientific Horiba XploRA+ Confocal Raman spectrometer with a 532 nm laser source. Samples were loaded on conductive, double-sided copper tape. For each sample, data were collected at 5 randomly selected spatially distant spots and averaged. Soft XAS measurements were performed at beamline 10-1 at the Stanford Synchrotron Radiation Lightsource (SSRL) of the SLAC National Accelerator Laboratory in total electron yield mode. The vertically polarized X-rays (sigma-polarization) were delivered to the sample in this experiment. The incident beam was monochromatized using a 600 line mm^{-1} spherical grating monochromator. *In situ* XAS measurements were performed at the Fe K-edge in transmission mode at SSRL beamline 2-2 of the SLAC National Accelerator Laboratory. The beamline was equipped with a Si (220) source, a 0.5 × 5 mm

beam size, an N_2 ion chamber gas, and ion chamber gains and offsets tuned using a reference Fe foil. Samples were placed in a 1 mm diameter quartz capillary diluted with mesoporous SiO_2 in a custom-built sample holder with graphite heating elements.[44] Sample temperature was measured with a K-type thermocouple inserted into the quartz capillary.

SUPPLEMENTAL INFORMATION

ACKNOWLEDGMENTS

AUTHOR CONTRIBUTIONS

E.S., G.W., and J.R. conceived the idea of using iron oxides for the low-temperature RWGS-CL reaction. E.S. synthesized samples and performed TGA experiments in the setup designed by J.R. and R.R. E.S., J.O., and M.G. performed packed-bed experiments. E.S., G.W., and A.V. performed XRD experiments. E.S. and G.W. performed *in situ* XAS experiments. G.W. performed soft XAS and TEM experiments. E.S. performed SEM/EDS experiments. S.M.-Q. performed XRF measurements. M.G. performed N_2 physisorption experiments. A.T., V.H., R.G., and A.M. supervised the project. E.S. wrote the manuscript, with input from all authors.

DECLARATION OF INTERESTS

The authors declare no competing interests.

REFERENCES

1. NOAA National Centers for Environmental Information (2022). State of the Climate: Global Climate Report for January 2022 (National Oceanic and Atmospheric Administration (NOAA)).

2. THE GLOBAL STATUS OF CCS: 2016 (2016)28 (Glob. CCS Inst.).

3. The Role of CCUS in Low-Carbon Power Systems, International Energy Agency, 49.

4. Daza, Y.A., and Kuhn, J.N. (2016). CO_2 conversion by reverse water gas shift catalysis: comparison of catalysts, mechanisms and their consequences for CO_2 conversion to liquid fuels. RSC Adv. 6, 49675–49691. https://doi.org/10.1039/C6RA05414E.

5. Liu, H.-X., Li, S.-Q., Wang, W.-W., Yu, W.-Z., Zhang, W.-J., Ma, C., and Jia, C.-J. (2022). Partially sintered copper–ceria as excellent catalyst for the high-temperature reverse water gas shift reaction. Nat. Commun. 13, 867. https://doi.org/10.1038/s41467-022-28476-5.

6. Tang, R., Zhu, Z., Li, C., Xiao, M., Wu, Z., Zhang, D., Zhang, C., Xiao, Y., Chu, M., Genest, A., et al. (2021). Ru-Catalyzed Reverse Water Gas Shift Reaction with Near-Unity Selectivity and Superior Stability. ACS Mater. Lett. 3, 1652–1659. https://doi.org/10.1021/acsmaterialslett.1c00523.

7. Lou, D., Zhu, Z., Xu, Y.-F., Li, C., Feng, K., Zhang, D., Lv, K., Wu, Z., Zhang, C., Ozin, G.A., et al. (2021). A core-shell catalyst design boosts the performance of photothermal reverse water gas shift catalysis. Sci. China Mater. 64, 2212–2220. https://doi.org/10.1007/s40843-020-1630-2.

8. Cui, X., and Kær, S.K. (2019). Thermodynamic Analyses of a Moderate-Temperature Process of Carbon Dioxide Hydrogenation to Methanol via Reverse Water–Gas Shift with In Situ Water Removal. Ind. Eng. Chem. Res. 58, 10559–10569. https://doi.org/10.1021/acs.iecr.9b01312.

9. Hydrogen Shot US Dep. Energy. https://www.energy.gov/eere/fuelcells/hydrogen-shot.

10. Galvita, V.V., Poelman, H., Bliznuk, V., Detavernier, C., and Marin, G.B. (2013). CeO_2-Modified Fe_2O_3 for CO_2 Utilization via Chemical Looping. Ind. Eng. Chem. Res. 52, 8416–8426. https://doi.org/10.1021/ie4003574.

11. Jin, B., Poelman, H., Detavernier, C., Liang, Z., Marin, G.B., and Galvita, V.V. (2021). Microstructured $ZrO2$ coating of iron oxide for enhanced $CO2$ conversion. Appl. Catal. B Environ. 292, 120194. https://doi.org/10.1016/j.apcatb.2021.120194.

12. Dharanipragada, N.V.R.A., Meledina, M., Galvita, V.V., Poelman, H., Turner, S., Van Tendeloo, G., Detavernier, C., and Marin, G.B. (2016). Deactivation Study of Fe_2O_3–CeO_2 during Redox Cycles for CO Production from CO_2. Ind. Eng. Chem. Res. 55, 5911–5922. https://doi.org/10.1021/acs.iecr.6b00963.

13. Hu, J., Galvita, V.V., Poelman, H., Detavernier, C., and Marin, G.B. (2017). A core-shell structured $Fe2O3/ZrO2@ZrO2$ nanomaterial with enhanced redox activity and stability for $CO2$ conversion. J. CO2 Util. 17, 20–31. https://doi.org/10.1016/j.jcou.2016.11.003.

14. Zeng, D., Qiu, Y., Ma, L., Li, M., Cui, D., Zhang, S., and Xiao, R. (2020). Tuning the Support Properties toward Higher CO_2 Conversion during a Chemical Looping Scheme. Environ. Sci. Technol. 54, 12467–12475. https://doi.org/10.1021/acs.est.0c01702.

15. Zhao, J., Xiong, Y., Gao, Z., Fu, F., Niu, L., and Jin, M. (2022). A La, Sm co-doped CeO_2 support for Fe_2O_3 to promote chemical looping splitting of CO_2 at moderate temperature. Sustain. Energy Fuels 6, 1448–1457. https://doi.org/10.1039/D1SE01957K.

16. Qiu, Y., Ma, L., Li, M., Cui, D., Zhang, S., Zeng, D., and Xiao, R. (2020). Copper and cobalt co-doped ferrites as effective agents for chemical looping $CO2$ splitting. Chem. Eng. J. 387, 124150. https://doi.org/10.1016/j.cej.2020.124150.

17. Daza, Y.A., Maiti, D., Kent, R.A., Bhethanabotla, V.R., and Kuhn, J.N. (2015). Isothermal reverse water gas shift chemical looping on La0.75Sr0.25Co(1−)Fe O3 perovskite-type oxides. Catal. Today 258, 691–698. https://doi.org/10.1016/j.cattod.2014.12.037.

18. Maiti, D., Hare, B.J., Daza, Y.A., Ramos, A.E., Kuhn, J.N., and Bhethanabotla, V.R. (2018). Earth abundant perovskite oxides for low temperature CO_2 conversion. Energy Environ. Sci. 11, 648–659. https://doi.org/10.1039/C7EE03383D.

19. Lee, M., Kim, Y., Lim, H.S., Jo, A., Kang, D., and Lee, J.W. (2020). Reverse Water–Gas Shift Chemical Looping Using a Core–Shell Structured Perovskite Oxygen Carrier. Energies 13, 5324. https://doi.org/10.3390/en13205324.

20. Hare, B.J., Maiti, D., Daza, Y.A., Bhethanabotla, V.R., and Kuhn, J.N. (2018). Enhanced CO_2 Conversion to CO by Silica-Supported Perovskite Oxides at Low Temperatures. ACS Catal. 8, 3021–3029. https://doi.org/10.1021/acscatal.7b03941.

21. Ramos, A.E., Maiti, D., Daza, Y.A., Kuhn, J.N., and Bhethanabotla, V.R. (2019). Co, Fe, and Mn in La-perovskite oxides for low temperature thermochemical $CO2$ conversion. Catal. Today 338, 52–59. https://doi.org/10.1016/j.cattod.2019.04.028.

22. Jo, A., Kim, Y., Lim, H.S., Lee, M., Kang, D., and Lee, J.W. (2022). Controlled template removal from nanocast La0.8Sr0.2FeO3 for enhanced $CO2$ conversion by reverse water–gas shift chemical looping. J. CO2 Util. 56, 101845. https://doi.org/10.1016/j.jcou.2021.101845.

23. Lim, H.S., Kim, Y., Kang, D., Lee, M., Jo, A., and Lee, J.W. (2021). Fundamental Aspects of Enhancing Low-Temperature CO_2 Splitting to CO on a Double La_2NiFeO6 Perovskite. ACS Catal. 11, 12220–12231. https://doi.org/10.1021/acscatal.1c03398.

24. Dharanipragada, N.V.R.A., Buelens, L.C., Poelman, H., De Grave, E., Galvita, V.V., and Marin, G.B. (2015). Mg–Fe–Al–O for advanced CO_2 to CO conversion: carbon monoxide yield vs. oxygen storage capacity. J. Mater. Chem. A 3, 16251–16262. https://doi.org/10.1039/C5TA02289D.

25. Ma, L., Qiu, Y., Li, M., Cui, D., Zhang, S., Zeng, D., and Xiao, R. (2020). Spinel-Structured Ternary Ferrites as Effective Agents for Chemical Looping CO_2 Splitting. Ind. Eng. Chem. Res. 59, 6924–6930. https://doi.org/10.1021/acs.iecr.9b06799.

26. Castellanos-Beltran, I.J., Perreault, L.-S., and Braidy, N. (2021). Application of Ni–Spinel in the Chemical-Looping Conversion of CO_2 to CO via Induction-Generated Oxygen Vacancies. J. Phys. Chem. C 125, 7213–7226. https://doi.org/10.1021/acs.jpcc.1c00928.

27. Rojas, J., Sun, E., Wan, G., Oh, J., Randall, R., Haribal, V., Jung, I.h., Gupta, R., and Majumdar, A. (2022). Iron-Poor Ferrites for Low-Temperature CO_2 Conversion via Reverse Water–Gas Shift Thermochemical Looping. ACS Sustain. Chem. Eng. 10, 12252–12261. https://doi.org/10.1021/acssuschemeng.2c03196.

28. Liu, Y., Qin, L., Cheng, Z., Goetze, J.W., Kong, F., Fan, J.A., and Fan, L.-S. (2019). Near 100% CO selectivity in nanoscaled iron-based oxygen carriers for chemical looping methane partial oxidation. Nat. Commun. 10, 5503. https://doi.org/10.1038/s41467-019-13560-0.

29. Zhu, X., Imtiaz, Q., Donat, F., Müller, C.R., and Li, F. (2020). Chemical looping beyond combustion – a perspective. Energy Environ. Sci. 13, 772–804. https://doi.org/10.1039/C9EE03793D.

30. Fan, L.-S. (2017). Chemical Looping Partial Oxidation: Gasification, Reforming, and Chemical Syntheses, 1st ed. (Cambridge University Press). https://doi.org/10.1017/9781108157841.

31. Fan, L.-S. (2017). Metal Oxide Oxygen Carriers. In Chemical Looping Partial Oxidation: Gasification, Reforming, and Chemical Syntheses Cambridge Series in Chemical Engineering (Cambridge University Press), pp. 55–171. https://doi.org/10.1017/9781108157841.003.

32. Makiura, J.-I., Kakihara, S., Higo, T., Ito, N., Hirano, Y., and Sekine, Y. (2022). Efficient CO_2 conversion to CO using chemical looping over Co–In oxide. Chem. Commun. 58, 4837–4840. https://doi.org/10.1039/D2CC00208F.

33. Hung, W.-Z., Law, Z.X., Tsai, D.-H., Chen, B.-H., Chen, C.-H., Hsu, H.-Y., and Pan, Y.-T. (2022). Selective $CO2$ deoxygenation to CO in chemically looped reverse water–gas shift using iron-based oxygen carrier. MRS Energy Sustain. 9, 342–349. https://doi.org/10.1557/s43581-022-00039-7.

34. Ma, Z., Watamaniuk, S.N.J., and Heinen, S.J. (2017). Kinetics of sintering induced surface area decay of iron oxide in the reduction process of chemical looping combustion. J. Vis. 17, 20–26. https://doi.org/10.1016/j.fuproc.2017.08.029.

35. Spreitzer, D., and Schenk, J. (2019). Reduction of Iron Oxides with Hydrogen—A Review. Steel Res. Int. 90, 1900108. https://doi.org/10.1002/srin.201900108.

36. Pineau, A., Kanari, N., and Gaballah, I. (2006). Kinetics of reduction of iron oxides by H2. Thermochim. Acta *447*, 89–100. https://doi.org/10.1016/j.tca.2005.10.004.

37. Hou, B., Zhang, H., Li, H., and Zhu, Q. (2012). Study on Kinetics of Iron Oxide Reduction by Hydrogen. Chin. J. Chem. Eng. *20*, 10–17. https://doi.org/10.1016/S1004-9541(12)60357-7.

38. Pineau, A., Kanari, N., and Gaballah, I. (2007). Kinetics of reduction of iron oxides by H2 Part II. Low temperature reduction of magnetite. Thermochim. Acta *14*.

39. Turkdogan, E.T., and Vinters, J.V. (1971). Gaseous reduction of iron oxides: Part I. Reduction of hematite in hydrogen. Metall. Trans. A *2*, 3175–3188. https://doi.org/10.1007/BF02814970.

40. Galinsky, N.L., Shafiefarhood, A., Chen, Y., Neal, L., and Li, F. (2015). Effect of support on redox stability of iron oxide for chemical looping conversion of methane. Appl. Catal. B Environ. *164*, 371–379. https://doi.org/10.1016/j.apcatb.2014.09.023.

41. Argyle, M., and Bartholomew, C. (2015). Heterogeneous Catalyst Deactivation and Regeneration: A Review. Catalysts *5*, 145–269. https://doi.org/10.3390/catal5010145.

42. Hu, J., Poelman, H., Marin, G.B., Detavernier, C., Kawi, S., and Galvita, V.V. (2020). FeO controls the sintering of iron-based oxygen carriers in chemical looping CO2 conversion. J. CO2 Util. *40*, 101216. https://doi.org/10.1016/j.jcou.2020.101216.

43. Galvita, V.V., Poelman, H., Detavernier, C., and Marin, G.B. (2015). Catalyst-assisted chemical looping for CO2 conversion to CO. Appl. Catal. B Environ. *164*, 184–191. https://doi.org/10.1016/j.apcatb.2014.09.007.

44. Hoffman, A.S., Singh, J.A., Bent, S.F., and Bare, S.R. (2018). *In situ* observation of phase changes of a silica-supported cobalt catalyst for the Fischer–Tropsch process by the development of a synchrotron-compatible *in situ/operando* powder X-ray diffraction cell. J. Synchrotron Radiat. *25*, 1673–1682. https://doi.org/10.1107/S1600577518013942.